

Guest metal-driven quantum anharmonic effects on stability and two-gap superconductivity in carbon-boron clathrates

Xianghui Meng,¹ Yanqing Shen,^{1,*} Xin Yang,¹ Xinyu Wang,¹ Qing Ai,^{2,†} Yong Shuai,^{2,‡} and Zhongxiang Zhou^{1,3,§}

¹*School of Physics, Harbin Institute of Technology, Harbin, 150001, China*

²*School of Energy Science and Engineering, Harbin Institute of Technology, Harbin 150001, China*

³*Heilongjiang Provincial Key Laboratory of Plasma Physics and Application Technology, Harbin Institute of Technology, Harbin 150001, China*

(Dated: December 8, 2025)

Traditionally, strong quantum anharmonic effects have been considered a characteristic of hydrogen-rich compounds. Here we propose that these effects also play a decisive role in boron-carbon clathrates. The stability and superconducting transition temperature (T_c) of carbon-boron clathrates XYB_6C_6 , whose metal atoms have an average oxidation state of +1.5, have long remained under debate. At this oxidation state, some combinations (e.g., $RbSrB_6C_6$) are dynamically stable, whereas others (e.g., $RbPbB_6C_6$) are not. Using the stochastic self-consistent harmonic approximation combined with machine learning, we find that the anharmonicity originates primarily from guest metal atoms. For comparison, we find that quantum fluctuations have negligible influence on SrB_3C_3 but remove the lattice instability of $RbPbB_6C_6$. The predicted T_c of $RbPbB_6C_6$ (≈ 88 K) is nearly twice that of SrB_3C_3 . Moreover, $RbPbB_6C_6$ exhibits two-gap superconductivity due to the higher C/B ratio in the density of states at the Fermi level compared to SrB_3C_3 , weakening the sp^3 hybridization. These findings demonstrate that quantum anharmonicity crucially governs the stability and superconductivity of XYB_6C_6 clathrates.

I. INTRODUCTION

Light-element-based materials have recently emerged as promising candidates for phonon-mediated superconductivity under ambient conditions, owing to their strong electron-phonon coupling (EPC) and tunable electronic structures [1–5]. The identification of many boron-carbon (B-C) materials has been primarily driven by theoretical predictions [6, 7], similar to the discovery process of high-pressure hydrides (e.g., H_3S , CaH_6 , LaH_{10} , $LaSc_2H_{24}$), which preceded experimental methods [8–11]. This research paradigm emphasizes the potential of first-principles methods, including crystal structure prediction (CSP) searches and EPC calculations [12–14], as invaluable tools to identify promising superconductors for future synthesis. A class of carbon-boron framework, initially pinpointed theoretically using CSP searches, has been synthesized in a host/guest clathrate structure [6, 7]. The SrB_3C_3 clathrate adopts the bipartite sodalite structure, where host cages are sp^3 -bonded truncated octahedral $C_{12}B_{12}$ framework that encapsulate Sr guest atoms. Among the first 57 elements of the periodic table ($X = H-La$), only Ca, Sr, Y, Ba, and La are capable of forming stable XB_3C_3 compounds under ambient pressure, with the critical temperature T_c consistently remaining below 50 K [15].

A key goal is to align the intrinsic properties of such materials with BCS theory (e.g., high density of states near the Fermi level, strong electron-phonon coupling, and high-frequency phonons) to address their low T_c issue [16]. Recent theoretical predictions for XYB_6C_6 , obtained when the metal atoms in XB_3C_3 are of two different elements, suggest that it could

achieve a higher T_c when the average oxidation state of XY is +1.5 [1]. However, the dynamical stability of XYB_6C_6 remains under debate. For example, when the average oxidation state of XY is +1.5, XYB_6C_6 ($XY = KSr, KCa, KPb, RbSr$) is dynamically stable. In contrast, XYB_6C_6 ($XY = RbPb, CsPb$) exhibits dynamical instability, especially when one of the X/Y elements is Pb. These uncertainties highlight the limitations of classical first-principles methods, particularly when quantum fluctuations significantly influence material behavior.

Quantum fluctuations raise concerns about the applicability of classical first-principles methods in predicting crystal structures and assessing the stability of hydrides [17–19]. Experimental results confirm that the $Fm\bar{3}m$ structure of LaH_{10} is the ground state at pressures between 137 and 218 GPa, contradicting theoretical predictions of lattice distortion [20]. Like LaH_{10} , XYB_6C_6 , with a sodalite-type structure with Pb as the X/Y element, may encounter similar stability issues. However, the stochastic self-consistent harmonic approximation (SSCHA) method used to simulate quantum fluctuations is computationally demanding [21]. Therefore, it is essential to introduce a new approach that combines SSCHA with machine learning (ML) techniques, establishing a novel standard for evaluating the stability of such materials.

In this work, we combine SSCHA with ML methods to investigate quantum anharmonicity in XYB_6C_6 . Specifically, quantum anharmonicity is closely related to the metal guest atoms in XYB_6C_6 and is particularly important for XYB_6C_6 with high EPC constants. The effect of anharmonicity on the dynamical stability and T_c of SrB_3C_3 is negligible. Anharmonicity is primarily driven by the heavy atom Pb, and we illustrate this using $RbPbB_6C_6$ as an example. After considering quantum anharmonic effects, the dynamical stability of $RbPbB_6C_6$ is significantly improved. By solving the anisotropic Migdal-Eliashberg equations, we further predict an EPC constant of 2.87 for $RbPbB_6C_6$ and calculate its T_c to be approximately 88 K, indicating its potential for high-

* shenyanqing2004@163.com

† hitaiqing@hit.edu.cn

‡ shuaiyong@hit.edu.cn

§ zhouxz@hit.edu.cn

temperature superconductivity.

II. COMPUTATIONAL DETAILS

First-principles calculations were conducted using the QUANTUM ESPRESSO package [22], implementing the generalized gradient approximation (GGA) as formulated by Perdew-Burke-Ernzerhof [23]. The energy cutoffs were set at 80 Ry for wavefunctions and 320 Ry for charge density and potential, employing optimized Norm-Conserving Vanderbilt pseudopotentials [24, 25]. Structural optimizations and self-consistent calculations were performed on a $10 \times 10 \times 10$ k-point grid within the Brillouin zone, adhering to stringent convergence criteria: 10^{-6} Ry for total energy and forces during ionic relaxation and 10^{-10} Ry for electronic convergence. Harmonic phonon properties were calculated using density functional perturbation theory on a $5 \times 5 \times 5$ q-point mesh.

The quantum zero-point motion and anharmonic effects were evaluated within the SSCHA framework [26]. To minimize the free energy, a finer stochastic sampling of 1000 configurations was employed at each iteration [27, 28]. A $2 \times 2 \times 2$ supercell containing 112 atoms was utilized to calculate the energy, forces, and stress, with the Monkhorst-Pack k-point grid scaled to $6 \times 6 \times 6$. To accelerate the prediction of energy, forces, and stress for each configuration, first-principles methods were combined with machine learning techniques. Machine learning interatomic potentials (MLIPs) were trained using a randomly selected training set of 200 structures and used to predict energy, forces, and stress for finer stochastic sampling in subsequent iterations. Anharmonic dynamical matrices were obtained on a commensurate $2 \times 2 \times 2$ q-point grid and interpolated to a $5 \times 5 \times 5$ q-point mesh, based on the difference between the harmonic and anharmonic dynamical matrices in the $2 \times 2 \times 2$ q-point grid.

The anisotropic Migdal-Eliashberg equation was solved using the EPW package, which integrates Maximally Localized Wannier Functions [14, 29]. A total of 24 sp^3 -hybridized states were constructed as MLWFs, each with a spatial spread below 1.55 Å. The Wannier interpolated results are shown in Figs. S1 and S2 of the Supplemental Material (SM) [30]. Electron-phonon matrix elements were interpolated over a dense $60 \times 60 \times 60$ k-point grid and a $20 \times 20 \times 20$ q-point grid. A Fermi surface window of 0.4 eV was selected to evaluate the states in the self-energy delta functions. Visualization of the Fermi surface was carried out using the FER-MISURFER package [31].

III. RESULTS AND DISCUSSION

Binary-guest C-B clathrates XYB_6C_6 are found to exist using CSP searches, allowing $X \neq Y$ [1, 6]. Similar to LaH_{10} [20, 32], quantum anharmonic effects play a crucial role in the stability and superconductivity of XYB_6C_6 , with Pb as the X/Y element. As an illustrative example, we consider sp^3 -bonded carbon-boron clathrates SrB_3C_3 and $RbPbB_6C_6$. Two cubic structures, SrB_3C_3 and $RbPbB_6C_6$, are depicted

in Figure 1, with structural parameters listed in Table S1 of SM [30].

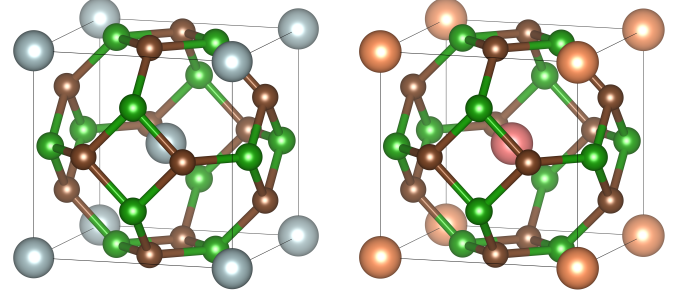


FIG. 1. Crystal structures for (a) SrB_3C_3 and (b) $RbPbB_6C_6$. The atoms are represented by silver, orange, red, green, and brown spheres, corresponding to Sr, Rb, Pb, B, and C, respectively.

As a first step, we assess their mechanical, dynamic, and thermodynamic stability. The elastic constants, summarized in Table S2 of the SM [30], satisfy the Born stability criteria for cubic systems: $C_{11} - C_{12} > 0$, $C_{11} + 2C_{12} > 0$, and $C_{44} > 0$ [33]. Minimizing the variational free energy requires a substantial number of single-point density functional theory calculations. Here, we employ MLIPs to compute forces, stresses, and energies. Figs. S3 and S4 display the errors

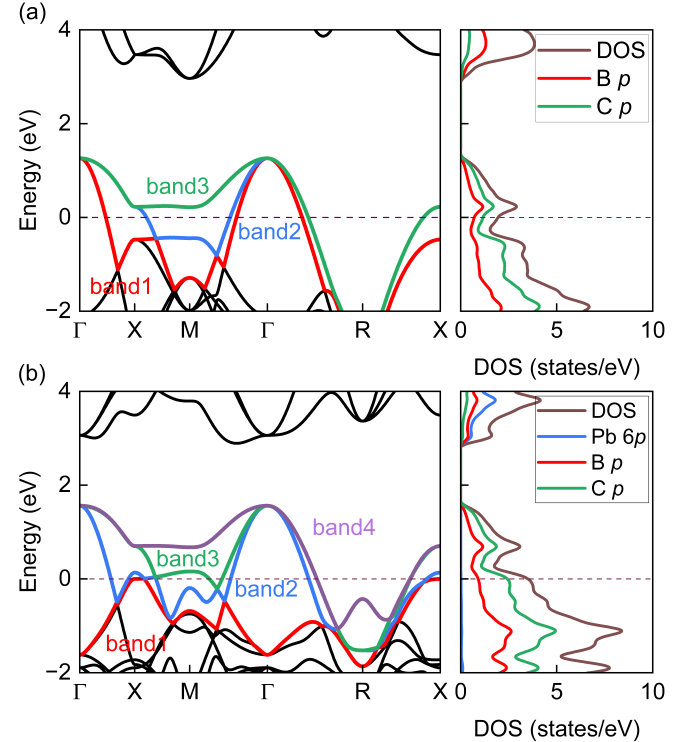


FIG. 2. The band structure and projected density of states for (a) SrB_3C_3 and (b) $RbPbB_6C_6$. In band structures, multiple bands dominated by nonmetal atoms that intersect with the Fermi level ($E_F = 0$ eV) are marked with different colors.

in force, energy, and stress calculations produced by MLIPs, which have less influence on SSCHA results due to averaging

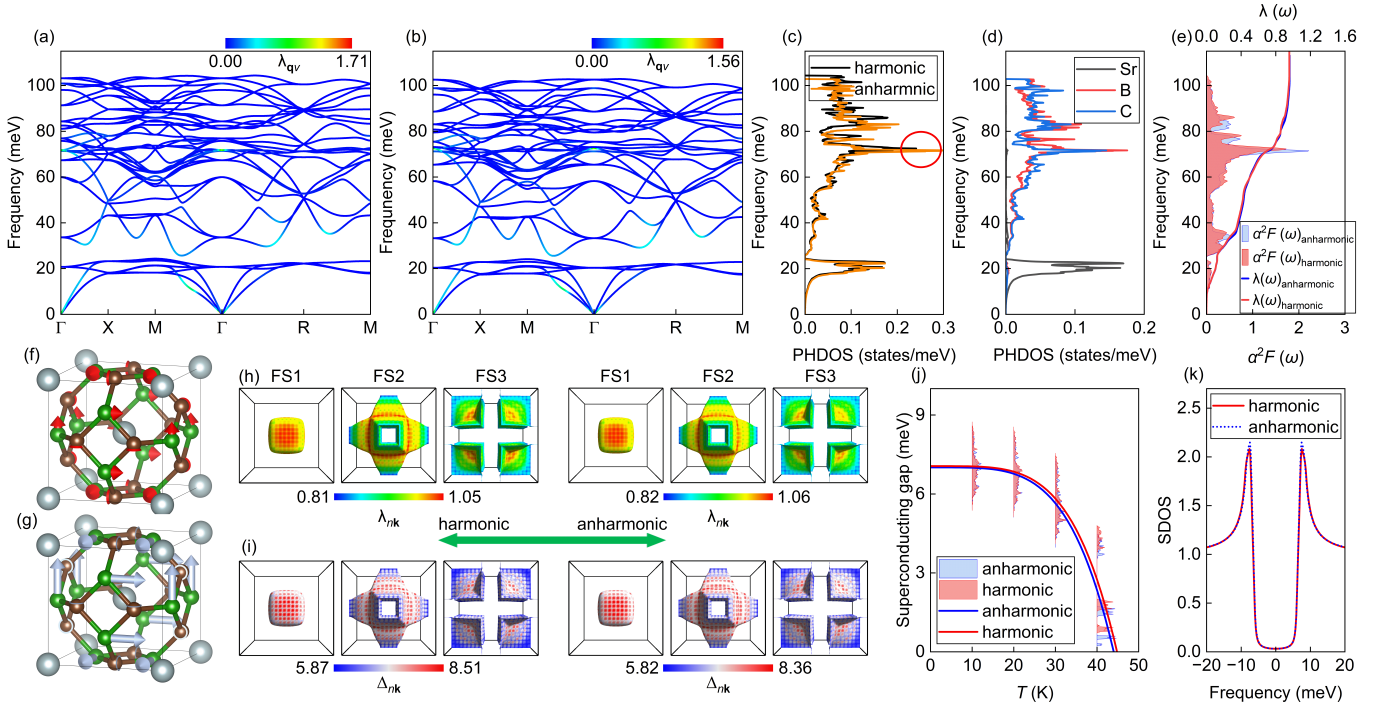


FIG. 3. Harmonic and anharmonic phonon properties and EPC of SrB₃C₃. (a) Harmonic phonon spectrum with λ_{qv} . (b) Anharmonic phonon spectrum with λ_{qv} . The color mapping from blue to red in panels (a) and (b) represents the magnitude of λ_{qv} for each phonon mode, with red indicating the highest values. (c) Harmonic and anharmonic phonon density of states (PHDOS). (d) Projected PHDOS on Sr, B, and C atoms in the anharmonic framework. (e) Eliashberg spectral function $\alpha^2 F(\omega)$ and cumulative EPC constant $\lambda(\omega)$. Double-degenerate E_g modes at the Γ point in (f) harmonic and (g) anharmonic frameworks. Displacements are shown by red and light blue arrows for the harmonic and anharmonic frameworks, respectively. (h) Momentum-resolved EPC strength λ_{nk} on the Fermi surface. (i) Superconducting gap Δ_{nk} on the Fermi surface at 10 K. (j) Temperature dependence of the superconducting gap Δ . (k) Superconducting density of states (SDOS) at 10 K.

effects [30]. Quantum effects arise from the guest atoms, with their strength dependent on the atomic species. After the inclusion of quantum anharmonic effects, the dynamical stability of SrB₃C₃ remains unchanged, while RbPbB₆C₆ becomes dynamically stable (see Fig. S5) [30]. SrB₃C₃ was synthesized at nearly 50 GPa and exists under ambient pressure in inert atmospheres [6]. Fig. S6 shows the computed formation enthalpy (ΔH) as functions of pressure for RbPbB₆C₆ [30]. It decomposes into RbC + Pb + 6B + 5C at pressures below 14.5 GPa, which is lower than the theoretical decomposition pressures of other analogous compounds [34]. Similarly, RbPbB₆C₆ may be obtained in a comparable manner as SrB₃C₃.

Figure 2 presents the electronic band structures and projected density of states (DOS) for SrB₃C₃ and RbPbB₆C₆. Three bands in SrB₃C₃, primarily derived from nonmetal atoms, intersect with the Fermi level ($E_F = 0$ eV) and are labeled with distinct colors (see Fig. 2(a)), in agreement with previous calculations [2, 15]. The DOS at the Fermi level plays a decisive role in determining T_c for this class of materials. Tuning the metal-guest atoms enables the alignment of E_F with regions of higher DOS. In RbPbB₆C₆, where the average metal oxidation state is +1.5, E_F shifts downward, crossing additional energy bands and increasing the DOS to 3.5 states/eV (see Fig. 2(b)). The states near E_F and the Fermi-surface pockets are dominated by B p and C p orbitals, with

the latter contributing more significantly owing to the higher electronegativity of carbon (see Figs. 2, S7, and S8 [30]). This p -orbital-dominated electronic character resembles that of layered boron-carbon intercalated compounds XB₂C₂ (X = Li, Na, K, etc.) [35–37]. The Fermi surface of RbPbB₆C₆ contains an additional sheet relative to SrB₃C₃, originating from the newly occupied bands induced by the downward shift of the Fermi level. This additional sheet reflects the enhanced electronic filling and is consistent with the increased DOS at the Fermi level.

Figures 3(a)-3(d) indicate that quantum anharmonic effects negligibly influence the phonon dispersions, the EPC strength λ_{qv} and the phonon density of states (PHDOS) for SrB₃C₃. The anharmonic PHDOS reveals that mid-to-high frequency vibrations are primarily associated with the lighter B and C atoms, while low-frequency modes are dominated by the heavier Sr atoms (see Fig. 3(d)). According to anharmonic PHDOS, we can infer that the EPC is dominated by B–C vibrations, similar to cage-like superconductors [38–40]. The total EPC constant $\lambda = 0.96$ remains unchanged between harmonic and anharmonic calculations, in good agreement with previous reports (0.92–1.02) [2, 15, 41, 42]. The cumulative $\lambda(\omega)$ increases in three distinct steps [Fig. 3(e)]: the first, contributed by acoustic and optical branches 1–3, accounts for $\approx 10.8\%$ of λ and reflects strong coupling along the M– Γ path, where the soft acoustic branch couples with electronic

states near E_F , similar to Na-intercalated boron carbide [36]; the second step arises from optical branches 7–9, contributing ≈ 0.41 to λ ; and the third is characterized by a distinct peak in $\alpha^2F(\omega)$ at ≈ 71 meV, originating from the doubly degenerate E_g modes at Γ (see Figs. 3(f) and 3(g)). These in-plane B vibrations within the B_2C_2 layer yield the largest λ_{qv} , analogous to the E_g modes in CaH_6 [9]. For comparison, the contributions of each phonon mode to EPC λ_v in both the harmonic and anharmonic approximations are shown in Fig. S9(a) [30]. The negligible identical λ_v values further confirm that quantum fluctuations exert minimal influence on SrB_3C_3 .

Quantum anharmonic effects have minimal impact on the anisotropy of λ_{nk} and Δ_{nk} , with $\lambda_{nk}(\max) - \lambda_{nk}(\min) = 0.24$ (anharmonic) vs. 0.24 (harmonic) and $\Delta_{nk}(\max) - \Delta_{nk}(\min) = 2.54$ meV (anharmonic) vs. 2.64 meV (harmonic) (see Figs. 3(h) and 3(i)). The anisotropy of SrB_3C_3 is comparable to that observed in hole-doped $(BN)_6$ and $NH_4B_2C_8$ [40, 43]. Fig. 3(j) shows that anharmonicity has a negligible effect on the temperature dependence of the superconducting gap Δ of SrB_3C_3 , with $T_c = 44$ K (anharmonic) vs. 44.81 K (harmonic) at the Morel-Anderson pseudopotential $\mu^* = 0.1$, in agreement with prior harmonic results [1, 2]. The normalized superconducting density of states (SDOS) at 10 K for both approximations are in excellent agreement, exhibiting a typical single-gap feature in SrB_3C_3 (see Fig. 3(k)). The single-gap feature is attributed to the sp^3 -hybridized σ states, similar to those in other cage-like superconductors, including hole-doped C_6 and C_{10} systems and $NH_4B_2C_8$ [39, 43].

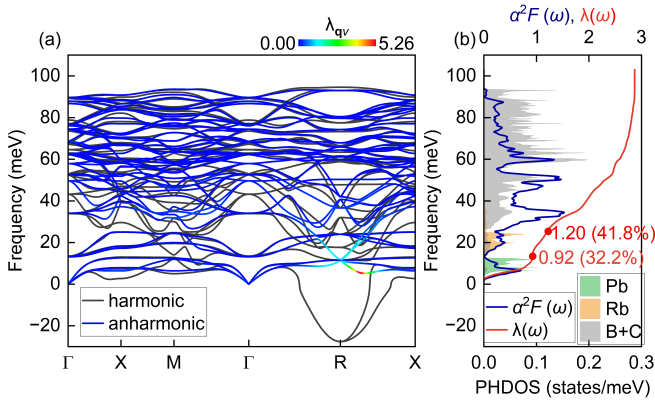


FIG. 4. Anharmonic phonon properties and EPC of $RbPbB_6C_6$. (a) Phonon spectrum. The color map from blue to red represents the magnitude of λ_{qv} for each phonon mode, with red denoting the highest coupling strengths. (b) Phonon density of states projected on Rb, Pb and the combined B+C atoms, Eliashberg spectral function $\alpha^2F(\omega)$, and integrated EPC strength $\lambda(\omega)$ in the anharmonic framework.

As shown in Fig. 4(a), the phonon dispersions for $RbPbB_6C_6$ are presented, comparing the harmonic and anharmonic results. Quantum anharmonic effects eliminate the imaginary frequencies, confirming dynamical stability of $RbPbB_6C_6$. In a similar manner, PdH exhibits unstable phonon spectra in harmonic calculations but stabilizes when anharmonic effects are included [44]. Compared to SrB_3C_3 ,

both the acoustic and low-lying optical branches (1–3) of $RbPbB_6C_6$ are markedly softened. Similar to $KSrB_6C_6$ and $KPbB_6C_6$ [1], which have an average metal oxidation state of +1.5, the softened modes near the R point show pronounced EPC contributions, particularly along the R–X path. This softening is accompanied by a marked increase in the mode-resolved EPC strength λ_v (see Fig. S9(b) [30]), resulting in a relatively high total EPC strength $\lambda \approx 2.87$ for $RbPbB_6C_6$. Total EPC strength λ of $RbPbB_6C_6$ exceeds that of SrB_3C_3 (0.96), $KPbB_6C_6$ (2.67) [1], and Fmmm $SrNH_4B_6C_6$ (2.01) [45]. In Fig. 4(b), the PHDOS for Pb, Rb, and B+C atoms, the Eliashberg function $\alpha^2F(\omega)$, and the integrated EPC strength $\lambda(\omega)$ are shown as a function of frequency. The acoustic branches are primarily driven by Pb vibrations, while the low-lying optical branches (1–3) are dominated by Rb motions, consistent with their respective atomic masses. For $\alpha^2F(\omega)$ and $\lambda(\omega)$, distinct contributions from different atoms (Pb, Rb, B + C) are observed. The first peak of $\alpha^2F(\omega)$ and the initial increase in $\lambda(\omega)$ originate from coupling between Pb vibrations and electrons near the Fermi surface. Notably, the second phase of $\lambda(\omega)$ is not associated with Rb motions. Although Rb dominates the PHDOS in the range 13.39–25.13 meV, the large λ_{qv} near the R point is primarily due to B and C vibrations, which are strongly coupled with the sp^3 hybridized σ -electrons (see Figs. 4(a) and S5(b) [30]). The higher optical branches (4–42) are mainly attributed to B and C vibrations, which contribute to the multiple peaks of $\alpha^2F(\omega)$ and the continuous increase in $\lambda(\omega)$ above 25.13 meV.

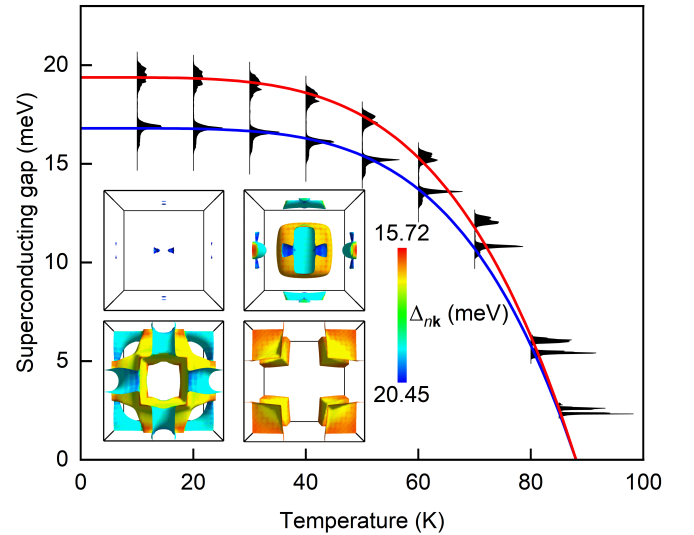


FIG. 5. Temperature dependence of the superconducting gap Δ for $RbPbB_6C_6$, obtained by solving the anisotropic Migdal-Eliashberg equation at $\mu^* = 0.1$. The inset shows the band- and momentum-resolved superconducting gap Δ_{nk} on the Fermi surface at 10 K, with the color scale indicating Δ_{nk} values ranging from 15.72 meV (blue) to 20.45 meV (red).

Figure 5 presents the temperature dependence of the superconducting gap Δ for $RbPbB_6C_6$ at $\mu^* = 0.1$. The two superconducting gaps decrease with increasing temper-

ature, closing simultaneously at $T_c = 88$ K. Anharmonic T_c of RbPbB_6C_6 exceeds that of SrB_3C_3 (40–45 K) [2, 15, 41, 42], RbYbB_6C_6 (67 K) [46], and Fmmm $\text{SrNH}_4\text{B}_6\text{C}_6$ (85 K) [45], comparable to that of hydrogen-modified alloy (42–77 K) [47–49]. At 10 K, the average values of the two superconducting gaps are 16.61 meV and 14.01 meV, corresponding to two distinct peaks in the SDOS, as shown in Fig. S10 [30]. The inset of Fig. 5 also presents Δ_{nk} on the Fermi surface (FS) at 10 K, with Δ_{nk} varying between 15.72 meV and 20.45 meV. This observation confirms that RbPbB_6C_6 is a two-gap superconductor, similar to MgB_2 and Janus MoSH [50, 51]. For RbPbB_6C_6 , the higher C/B ratio in the density of states at the Fermi level compared to SrB_3C_3 , weakens sp^3 hybridization, leading to electronic states dominated by C and B characteristics, each opening a distinct gap. Importantly, larger values of Δ_{nk} on the FS are found to correlate with higher EPC strength λ_{nk} , as shown in Fig. S11 [30], further supporting the phonon-mediated nature of superconductivity in RbPbB_6C_6 . The largest gap, observed on FS4, is attributed to Pb phonon modes with strong EPC along the R–X direction.

IV. CONCLUSIONS

In conclusion, we demonstrate the crucial role of quantum effects in determining the stability and superconductivity of binary-guest carbon-boron clathrates XYB_6C_6 , challenging harmonic-level predictions and evidencing flaws in previous studies. Quantum effects are induced by the guest atoms, with their magnitude depending on the atomic species. For SrB_3C_3 , quantum effects have little impact on its dynamical stability and T_c . In contrast, pronounced quantum effects arise when Pb is one of the X/Y elements. Including quantum effects stabilizes RbPbB_6C_6 and raises T_c to 88 K, nearly twice that of SrB_3C_3 (44 K). The enhanced T_c originates from two key factors: (1) the lower oxidation state of RbPb, which shifts the Fermi level downward, thereby increasing DOS at the Fermi level, and (2) the softened phonon modes, both of which collectively strengthens the electron-phonon coupling of 2.87. These findings provide a reliable framework for assessing dynamical stability and superconducting T_c in carbon-boron clathrates exhibiting strong quantum anharmonic effects.

V. ACKNOWLEDGMENTS

We acknowledge the support by National Natural Science Foundation of China (No.52227813, No.11204053 and No.11074059).

-
- [1] N. Geng, K. P. Hilleke, L. Zhu, X. Wang, T. A. Strobel, and E. Zurek, Conventional high-temperature superconductivity in metallic, covalently bonded, binary-guest C–B clathrates, *Journal of the American Chemical Society* **145**, 1696 (2023).
 - [2] J.-N. Wang, X.-W. Yan, and M. Gao, High-temperature superconductivity in SrB_3C_3 and BaB_3C_3 predicted from first-principles anisotropic migdal-eliasberg theory, *Phys. Rev. B* **103**, 144515 (2021).
 - [3] Y.-L. Hai, M.-J. Jiang, H.-L. Tian, G.-H. Zhong, W.-J. Li, C.-L. Yang, X.-J. Chen, and H.-Q. Lin, Superconductivity above 100 K predicted in carbon-cage network, *Advanced Science* **10**, 2303639 (2023).
 - [4] H.-B. Ding, R. Niu, S.-A. Li, Y.-M. Liu, X.-J. Chen, H.-Q. Lin, and G.-H. Zhong, Hydrogen-doped c-bn as a promising path to high-temperature superconductivity above 120 K at ambient pressure, *Advanced Science* **11**, 2408275 (2024).
 - [5] N. Geng, G. J. Scilla, and E. Zurek, Theoretical predictions of MB_5N_5 : Atom-stuffed boronitride clathrate cages derived from the high-pressure superhydrides, *Materials Today Physics* **55**, 101732 (2025).
 - [6] L. Zhu, G. M. Borstad, H. Liu, P. A. Guńka, M. Guertte, J.-A. Dolyniuk, Y. Meng, E. Greenberg, V. B. Prakapenka, B. L. Chaloux, *et al.*, Carbon-boron clathrates as a new class of sp^3 -bonded framework materials, *Science advances* **6**, eaay8361 (2020).
 - [7] T. A. Strobel, L. Zhu, P. A. Guńka, G. M. Borstad, and M. Guertte, A lanthanum-filled carbon–boron clathrate, *Angewandte Chemie* **133**, 2913 (2021).
 - [8] D. Duan, Y. Liu, F. Tian, D. Li, X. Huang, Z. Zhao, H. Yu, B. Liu, W. Tian, and T. Cui, Pressure-induced metallization of dense $(\text{H}_2\text{S})_2\text{H}_2$ with high- T_c superconductivity, *Scientific reports* **4**, 6968 (2014).
 - [9] H. Wang, J. S. Tse, K. Tanaka, T. Iitaka, and Y. Ma, Superconductive sodalite-like clathrate calcium hydride at high pressures, *Proceedings of the National Academy of Sciences* **109**, 6463 (2012).
 - [10] F. Peng, Y. Sun, C. J. Pickard, R. J. Needs, Q. Wu, and Y. Ma, Hydrogen clathrate structures in rare earth hydrides at high pressures: Possible route to room-temperature superconductivity, *Phys. Rev. Lett.* **119**, 107001 (2017).
 - [11] X.-L. He, W. Zhao, Y. Xie, A. Hermann, R. J. Hemley, H. Liu, and Y. Ma, Predicted hot superconductivity in $\text{LaSc}_2\text{H}_{10}$ under pressure, *Proceedings of the National Academy of Sciences* **121**, e2401840121 (2024).
 - [12] A. O. Lyakhov, A. R. Oganov, H. T. Stokes, and Q. Zhu, New developments in evolutionary structure prediction algorithm uspeX, *Computer Physics Communications* **184**, 1172 (2013).
 - [13] Y. Wang, J. Lv, L. Zhu, and Y. Ma, Calypso: A method for crystal structure prediction, *Computer Physics Communications* **183**, 2063 (2012).
 - [14] H. Lee, S. Poncé, K. Bushick, S. Hajinazar, J. Lafuente-Bartolome, J. Leveillee, C. Lian, J.-M. Lihm, F. Macheda, H. Mori, *et al.*, Electron–phonon physics from first principles using the epw code, *npj Computational Materials* **9**, 156 (2023).

- [15] S. Di Cataldo, S. Qulaghasi, G. B. Bachelet, and L. Boeri, High- T_c superconductivity in doped boron-carbon clathrates, *Phys. Rev. B* **105**, 064516 (2022).
- [16] J. Bardeen, L. N. Cooper, and J. R. Schrieffer, Theory of superconductivity, *Phys. Rev.* **108**, 1175 (1957).
- [17] R. Lucrezii, P. P. Ferreira, M. Aichhorn, and C. Heil, Temperature and quantum anharmonic lattice effects on stability and superconductivity in lutetium trihydride, *Nature Communications* **15**, 441 (2024).
- [18] F. Belli and E. Zurek, Efficient modelling of anharmonicity and quantum effects in PdCuH₂ with machine learning potentials, *npj Computational Materials* **11**, 87 (2025).
- [19] P. Hou, Y. Ma, H. Xie, M. Li, Y. Cai, Y. Shen, X. Wang, and M. Pang, Significant impact of quantum and anharmonic effects on the structural stability and superconductivity of NbH₃ at high pressures, *Phys. Rev. B* **112**, 104110 (2025).
- [20] I. Errea, F. Belli, L. Monacelli, A. Sanna, T. Koretsune, T. Tadano, R. Bianco, M. Calandra, R. Arita, F. Mauri, *et al.*, Quantum crystal structure in the 250-kelvin superconducting lanthanum hydride, *Nature* **578**, 66 (2020).
- [21] L. Monacelli, R. Bianco, M. Cherubini, M. Calandra, I. Errea, and F. Mauri, The stochastic self-consistent harmonic approximation: calculating vibrational properties of materials with full quantum and anharmonic effects, *Journal of Physics: Condensed Matter* **33**, 363001 (2021).
- [22] P. Giannozzi, O. Baseggio, P. Bonfà, D. Brunato, R. Car, I. Carnimeo, C. Cavazzoni, S. de Gironcoli, P. Delugas, F. Ferrari Ruffino, A. Ferretti, N. Marzari, I. Timrov, A. Urru, and S. Baroni, Quantum espresso toward the exascale, *The Journal of Chemical Physics* **152**, 154105 (2020).
- [23] J. P. Perdew, K. Burke, and M. Ernzerhof, Generalized gradient approximation made simple, *Phys. Rev. Lett.* **77**, 3865 (1996).
- [24] D. R. Hamann, Optimized norm-conserving vanderbilt pseudopotentials, *Phys. Rev. B* **88**, 085117 (2013).
- [25] M. J. Van Setten, M. Giantomassi, E. Bousquet, M. J. Verstraete, D. R. Hamann, X. Gonze, and G.-M. Rignanese, The pseudodojo: Training and grading a 85 element optimized norm-conserving pseudopotential table, *Computer Physics Communications* **226**, 39 (2018).
- [26] I. Errea, M. Calandra, C. J. Pickard, J. R. Nelson, R. J. Needs, Y. Li, H. Liu, Y. Zhang, Y. Ma, and F. Mauri, Quantum hydrogen-bond symmetrization in the superconducting hydrogen sulfide system, *Nature* **532**, 81 (2016).
- [27] A. Glielmo, P. Sollich, and A. De Vita, Accurate interatomic force fields via machine learning with covariant kernels, *Phys. Rev. B* **95**, 214302 (2017).
- [28] A. V. Shapeev, Moment tensor potentials: A class of systematically improvable interatomic potentials, *Multiscale Modeling & Simulation* **14**, 1153 (2016).
- [29] G. Pizzi, V. Vitale, R. Arita, S. Blügel, F. Freimuth, G. Géranton, M. Gibertini, D. Gresch, C. Johnson, T. Koretsune, *et al.*, Wannier90 as a community code: new features and applications, *Journal of Physics: Condensed Matter* **32**, 165902 (2020).
- [30] See supplemental materials for wannier-interpolated electronic band structures and phonon spectrums, structural parameters, mechanical properties, machine learning, anharmonic phonon spectrums with atomic vibrational contributions, formation enthalpy, fermi surfaces, mode-resolved electron-phonon coupling constants λ_v , band- and momentum-resolved epc strength λ_{nk} on the fermi surface, normalized superconducting density of states for SrB₃C₃ and RbPbB₆C₆.
- [31] M. Kawamura, Fermisurfer: Fermi-surface viewer providing multiple representation schemes, *Computer Physics Communications* **239**, 197 (2019).
- [32] C. Tantardini, A. G. Kvashnin, M. Giantomassi, M. Iliaš, B. I. Yakobson, R. J. Hemley, and X. Gonze, Charge density waves and structural phase transition in the high- T_c superconducting LaH₁₀ quantum crystal, *Phys. Rev. B* **112**, 115154 (2025).
- [33] F. Mouhat and F. m. c.-X. Coudert, Necessary and sufficient elastic stability conditions in various crystal systems, *Phys. Rev. B* **90**, 224104 (2014).
- [34] W. Cui, T. Bi, J. Shi, Y. Li, H. Liu, E. Zurek, and R. J. Hemley, Route to high- T_c superconductivity via CH₄-intercalated H₃S hydride perovskites, *Phys. Rev. B* **101**, 134504 (2020).
- [35] M. Gao, X.-W. Yan, Z.-Y. Lu, and T. Xiang, Strong-coupling superconductivity in LiB₂C₂ trilayer films, *Phys. Rev. B* **101**, 094501 (2020).
- [36] X. Meng, Y. Shen, L. Lv, M. Zhou, X. Yang, Y. Zhang, L. Pang, P. E, and Z. Zhou, Unraveling the evolution of multigap superconductivity in layered Na-B-C films: An additional energy gap induced by the internal B-C layer, *Materials Today Physics* **47**, 101532 (2024).
- [37] H.-D. Liu, X.-P. Fu, Z.-G. Fu, H.-Y. Lu, and P. Zhang, High- T_c and three-gap two-dimensional superconductors with electronic and phononic topology: kb₂c₂, *Phys. Rev. B* **111**, 184502 (2025).
- [38] C. Chen, J. Miao, J. Zuo, S. He, and C. Lu, Superconductivity of metal doped-boron-nitrogen clathrates under ambient pressure, *Phys. Rev. B* **110**, 174514 (2024).
- [39] Y.-L. Han, K.-Y. Jiang, B.-T. Wang, P. Zhang, and H.-Y. Lu, Ambient-pressure superconductivity above 100 K in hole-doped carbon clathrates with superior hardness, *Phys. Rev. B* **110**, 104504 (2024).
- [40] Y.-L. Han, K.-Y. Jiang, B.-T. Wang, P. Zhang, and H.-Y. Lu, Anisotropic high- T_c superconductivity above 90 K in hole-doped boron-nitrogen clathrates at ambient pressure, *Phys. Rev. B* **111**, 094520 (2025).
- [41] L. Zhu, H. Liu, M. Somayazulu, Y. Meng, P. A. Guíka, T. B. Shiell, C. Kenney-Benson, S. Chariton, V. B. Prakapenka, H. Yoon, J. A. Horn, J. Paglione, R. Hoffmann, R. E. Cohen, and T. A. Strobel, Superconductivity in SrB₃C₃ clathrate, *Phys. Rev. Res.* **5**, 013012 (2023).
- [42] P. Zhang, X. Li, X. Yang, H. Wang, Y. Yao, and H. Liu, Path to high- T_c superconductivity via Rb substitution of guest metal atoms in the SrB₃C₃ clathrate, *Phys. Rev. B* **105**, 094503 (2022).
- [43] S. Y. Y. X. W. C. A. Q. S. Y. Meng, Xianghui and Z. Zhou, Effects of anharmonic phonons on superconductivity in the nh₄-intercalated boron-carbon clathrate nh₄b₂c₈, *Phys. Rev. B* , (2025).
- [44] I. Errea, M. Calandra, and F. Mauri, First-principles theory of anharmonicity and the inverse isotope effect in superconducting palladium-hydride compounds, *Phys. Rev. Lett.* **111**, 177002 (2013).
- [45] Y. Sun and L. Zhu, Hydride units filled boron-carbon clathrate: a pathway for high-temperature superconductivity at ambient pressure, *Communications Physics* **7**, 324 (2024).
- [46] Q. Duan, L. Zhan, J. Shen, X. Zhong, and C. Lu, Predicting superconductivity near 70 K in 1166-type boron-carbon clathrates at ambient pressure, *Phys. Rev. B* **109**, 054505 (2024).
- [47] C. Tian, Y. He, Y.-h. Zhu, J. Du, S.-m. Liu, W.-h. Guo, H.-x. Zhong, J. Lu, X. Wang, and J.-j. Shi, Few-hydrogen metal-bonded perovskite superconductor MgHCu₃ with a critical temperature of 42 K under atmospheric pressure, *Advanced Functional Materials* **34**, 2304919 (2024).
- [48] C. Tian, Y.-h. Zhu, J. Du, H.-x. Zhong, J. Lu, X. Wang, and J.-j. Shi, Ductile copper-based hydride superconductors at tc 60 k with a new paradigm under ambient pressure, *Superconductor*

- [Science and Technology](#) **38**, 075015 (2025).
- [49] C. Tian, Y.-h. Zhu, J. Du, H.-x. Zhong, J. Lu, X. Wang, and J.-j. Shi, Ductile copper hydride eliashberg superconductors with T_c in the liquid-nitrogen temperature range and band topology at ambient pressure, [Mater. Horiz.](#) **12**, 4851 (2025).
- [50] E. R. Margine and F. Giustino, Anisotropic migdal-eliashberg theory using wannier functions, [Phys. Rev. B](#) **87**, 024505 (2013).
- [51] P.-F. Liu, F. Zheng, J. Li, J.-G. Si, L. Wei, J. Zhang, and B.-T. Wang, Two-gap superconductivity in a janus mosh monolayer, [Phys. Rev. B](#) **105**, 245420 (2022).